Received: 1 March 2019 | Revised: 14 August 2019 | Accepted: 15 August 2019

DOI: 10.1002/mrm.27985

FULL PAPER

Magnetic Resonance in Medicine

Field drift correction of proton resonance frequency shift temperature mapping with multichannel fast alternating nonselective free induction decay readouts

Cyril J. Ferrer[1] | Lambertus W. Bartels[1] | Tijl A. van der Velden[1] | Holger Grüll[2] | Edwin Heijman[2,3] | Chrit T. W. Moonen[1] | Clemens Bos[1]

[1]Imaging Division, University Medical Center Utrecht, Utrecht, Netherlands

[2]University of Cologne, Faculty of Medicine and University Hospital of Cologne, Department of Diagnostic and Interventional Radiology, Cologne, Germany

[3]Oncology Solutions, Philips Research, Aachen, Germany

Correspondence
Cyril Ferrer, Imaging Division, University Medical Center Utrecht, Heidelberglaan 100, Utrecht, Utrecht 3584 CX, Netherlands.
Email: C.J.Ferrer@umcutrecht.nl

Funding information
FP7 International Cooperation, Grant/Award Number: 603028; European Union Seventh Framework Programme, Grant/Award Number: FP7/2007–2013

Purpose: To demonstrate that proton resonance frequency shift MR thermometry (PRFS-MRT) acquisition with nonselective free induction decay (FID), combined with coil sensitivity profiles, allows spatially resolved B_0 drift-corrected thermometry.

Methods: Phantom experiments were performed at 1.5T and 3T. Acquisition of PRFS-MRT and FID were performed during MR-guided high-intensity focused ultrasound heating. The phase of the FIDs was used to estimate the change in angular frequency $\delta\omega_{drift}$ per coil element. Two correction methods were investigated: (1) using the average $\delta\omega_{drift}$ over all coil elements (0th-order) and (2) using coil sensitivity profiles for spatially resolved correction. Optical probes were used for independent temperature verification. In-vivo feasibility of the methods was evaluated in the leg of 1 healthy volunteer at 1.5T.

Results: In 30 minutes, B_0 drift led to an apparent temperature change of up to –18°C and –98°C at 1.5T and 3T, respectively. In the sonicated area, both corrections had a median error of 0.19°C at 1.5T and –0.54°C at 3T. At 1.5T, the measured median error with respect to the optical probe was –1.28°C with the 0th-order correction and improved to 0.43°C with the spatially resolved correction. In vivo, without correction the spatiotemporal median of the apparent temperature was at –4.3°C and interquartile range (IQR) of 9.31°C. The 0th-order correction had a median of 0.75°C and IQR of 0.96°C. The spatially resolved method had the lowest median at 0.33°C and IQR of 0.80°C.

Conclusion: FID phase information from individual receive coil elements allows spatially resolved B_0 drift correction in PRFS-based MRT.

KEYWORDS
B_0 field control, B_0 field drift, coil sensitivity, FID, PRFS thermometry, receiver coil array

1 | INTRODUCTION

MR-guided high-intensity focused ultrasound (MR-HIFU) is an emerging technology for noninvasive thermal treatment of various tumors.[1] Currently, thermal ablation of uterine fibroids, prostate cancer, metastatic bone tumors, and part of the thalamus to treat neurological disorders (i.e., essential tremor) are the main clinical applications of MR-HIFU.[2-4] Whereas ablation therapies aiming at the induction of tumor necrosis have been used clinically, other forms of thermal treatment are under investigation for oncological applications.[5,6] One example is the creation of local mild hyperthermia induced by volumetric HIFU heating for triggering drug release from thermosensitive carriers[7,8] or for chemo- or radiosensitization.[9] Recently, the first clinical evidence of volumetric mild hyperthermia for targeted local drug delivery in soft-tissue sarcoma has been presented, illustrating the interest for this therapeutic option.[10]

For noninvasive therapy, image guidance plays an important role in accurate tumor targeting and therapy monitoring. Both ultrasound (US) and MRI guidance have been used for thermal HIFU therapies.[11] A key advantage of MRI above US guidance is the possibility to acquire temperature maps to monitor changes in the spatiotemporal temperature distribution in almost real time. Proton resonance frequency shift (PRFS) MR thermometry (MRT) is commonly used for guidance of MR-HIFU procedures.[12,13] In the context of mild hyperthermia, where the aim is to create temporally and spatially homogeneous mild heating in the target area, information about the temperature distribution is necessary to avoid thermal damage and for feedback control.[14-16]

MRT is done by measurement of phase changes in gradient echo MR images to detect changes in the proton resonance frequency caused by heating in aqueous tissues. Phase differences between a current phase image acquired during heating and a reference phase image acquired before heating are converted to relative temperature maps, making use of the known sensitivity of the proton resonance frequency to temperature changes.[17]

Mild hyperthermia requires temperature mapping over extensive periods of time. But long-term dynamic scanning may lead to B_0 field drift, which is known to be caused by hardware imperfections (e.g., coupling between gradient and shim coils, gradient switching, and eddy currents and field fluctuations, e.g., changes in cryogen level, heating of ferromagnetic passive shim elements). This drift leads to systematic errors in PRFS measurements and can compromise MRT.[12] In a multivendor study, it has been demonstrated that B_0 drift depends on the previous and current scanner activity and is spatially nonuniform.[18]

Several approaches have been suggested, to correct for spatiotemporal variations in B_0. The phase of the fat signal, which is temperature independent, has been investigated for correction of B_0 field disturbances using body or external fat reference signals.[19-21] Another group of previously developed B_0 correction methods is based on phase navigator echoes or free induction decay (FID) phase signals and was mainly developed to compensate for motion-induced B_0 variations.[22,23] In these reports, the FID signal is acquired after slice excitation prior to or after image acquisition.

Whereas the B_0 drift affects the phase in the whole field of view, the phase changes induced by HIFU heating are highly localized.[12,13] The so-called referenceless PRFS methods make use of that property, by determining the phase background from the acquired phase map during heating. Provided a homogeneous phase region of interest (ROI) surrounding the target that remains at reference temperature is available, referenceless MRT allows to reduce the sensitivity to field drift effects using the current phase maps only.[24] Multiple approaches based on different background field fitting constraints have been proposed.[25-27] Recently, a comparison study illustrated limitations and advantages of 5 of these methods.[28]

Arrays of field probes, which are positioned outside the patient, have also been proposed to introduce spatiotemporal field stabilization based on real-time sensing and feedback control.[29,30] Recently, the use of field probes has been proposed for drift correction of PRFS temperature mapping, but this approach required the use of additional hardware.[31]

In this study, the proposed method makes use of 2 key concepts. First, like the basis of referenceless MRT[26] as well as previously proposed slice-selective FID navigator approaches for B_0 field drift correction,[32] we assume that HIFU heating is highly localized. Given that the B_0 field drift correction of MRT is introduced here, the same assumption is made, but we argue that using the phase signal from the complete sample will reduce sensitivity to temperature-induced phase changes. Second, we suggest to combine the information of the individual coil elements to retrieve spatial information on the B_0 drift, by making use of the coil sensitivity profiles. Therefore, we propose a methodology to use the coil sensitivity profiles (as described in the sensitivity encoding methodology) combined with nonselective FIDs acquired during thermal treatment to correct PRFS-based temperature mapping for the spatiotemporal B_0 drift. The correction method will be investigated in MR-HIFU phantom experiments at 1.5T and 3T. An in-vivo experiment without HIFU heating will be performed at 1.5T. In all experiments, the proposed method will be compared to a state-of-the-art referenceless PRFS method.

2 | METHODS

The typical implementation of PRFS-MRT requires a reference and current phase image for phase subtraction. As shown in Figures 1 and 2A, we suggest to acquire a

set of reference FIDs in a preintervention step and continuously acquire FIDs during the intervention. FIDs will then be processed for B_0 drift correction, either allowing a 0th-order correction or in combination with coil sensitivity profiles acquired at the start of the procedure to resolve spatial variations in B_0 drift.

2.1 | Calculation of temperature maps

In PRFS thermometry, maps of the temperature change ΔT are obtained from the phase difference $\Delta\varphi$ (in rad) between the incoming phase and reference phase image[12] (Equation 1):

$$\Delta T(x,y) = \frac{\Delta\varphi(x,y)}{2\pi \propto TE\bar{\gamma}B_0}, \quad (1)$$

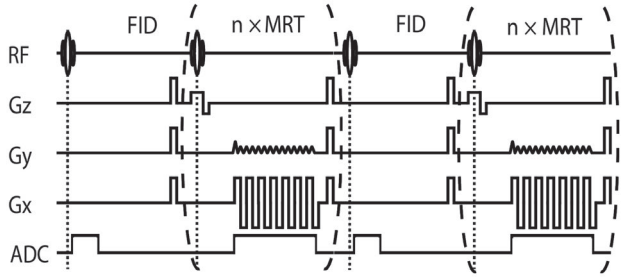

FIGURE 1 Schematic pulse diagram of the fast alternating full volume non-selective excitation FID and PRFS-MRT acquisition (n is the number of repetitions required to acquire all slices for 1 dynamic). ADC = analog to digital converter

where (x, y) are indices in the acquired phase maps, α is the temperature coefficient of the shielding constant (–0.01 10^{-6}/°C), B_0 the main magnetic field in T, the TE in seconds, and $\bar{\gamma}$ the ^{1}H gyromagnetic ratio 42.58 MHz/T.

2.2 | B_0 drift estimation

A nonselective block pulse was used to excite the full volume and generate an FID (Figures 1 and 2A). An estimate for δT_{drift}, the error in the temperature map attributable to B_0 drift can then be obtained from the FIDs. For each receiver channel, the FID signal is a summation of all signal contributions, weighted by sensitivity of the coil element. Therefore, the phase evolution over the current FID was compared to the phase evolution of a reference FID to estimate the B_0 drift. As illustrated in Figure 2B, the phase difference for each coil element n was calculated as follows (Equation 2):

$$\delta\varphi_n(t_i) = \varphi_{n,t}(t_i) - \varphi_{n,t_{ref}}(t_i) \quad (2)$$

where $\delta\varphi_n$ is in rad, t_i is the time of the i^{th} sample during the FID signal acquisition, $\varphi_{n,t}$ is the phase evolution of the FID signal acquired during heating in rad, and $\varphi_{n,t_{ref}}$ the phase evolution of the reference FID acquired in a previous heating step.

For each coil element n, the phase difference of the FIDs over time $\delta\varphi_n(t_i)$ can be described with a linear model from which the angular frequency drift $\delta\omega_{drift,n}$ can be obtained (Equation 3):

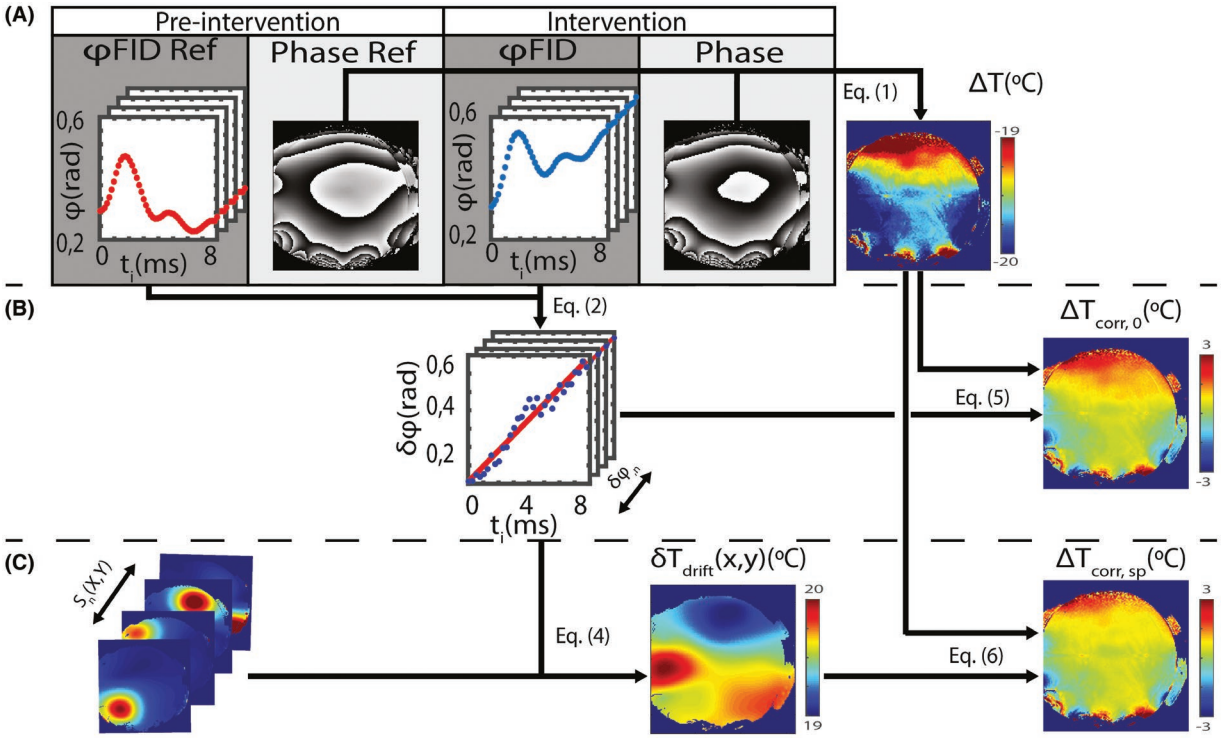

FIGURE 2 A, The data generated by the alternating PRFS-MRT/FID acquisition scheme and PRFS-based MRT calculation, B, the processing steps to calculate and apply the 0th-order correction, and C, the processing steps to calculate and apply the spatially resolved correction

$$\delta\varphi_n\left(t_i\right)=\delta\omega_{drift,n}.t_i \tag{3}$$

where the unknown $\delta\omega_{drift,n}$ is the angular frequency offset in rad.s^{-1} and hence, $\delta\omega_{drift,n}$ was obtained by a linear least squares fit of Equation 3 to the phase difference of the samples.

2.2.1 | Spatially resolved frequency estimates

As illustrated in Figure 2C, to retrieve spatial information, sensitivity profiles are used to create a spatially resolved frequency drift correction $\delta\omega_{drift}(x, y)$ as follows (Equation 4):

$$\delta\omega_{drift}(x,y)=\frac{\sum_{n=0}^{N}S_n(x,y)\times\delta\omega_{drift,n}}{\sum_{n=0}^{N}S_n(x,y)} \tag{4}$$

where S is the magnitude from the coil sensitivity profile acquired from a reference scan, as defined by Pruessmann et al[33]; N is the total number of coil element with the used system.

2.2.2 | 0th-order correction

From Equation 3, a 0th-order field drift estimate is then obtained by averaging $\delta\omega_{drift,n}$ over all coil elements and used to correct the temperature maps as follows (Equation 5):

$$\Delta T_{corr,0}(x,y)=\Delta T(x,y)-\overline{\delta \mathrm{T}_{drift,n}}\ \text{with}\ \delta \mathrm{T}_{drift,n}=\frac{\delta\omega_{drift,n}}{2\pi\propto\bar{\gamma}B_0} \tag{5}$$

where $\overline{\delta \mathrm{T}_{drift,n}}$ is the average $\delta T_{drift,n}$ over the number or coil elements n and is $\bar{\gamma}$ the ^{1}H gyromagnetic ratio 42.58MHz/T.

2.2.3 | Spatially resolved correction

From Equation 4, the spatially resolved frequency estimates can be interpreted as temperature to correct for drift effects (Equation 6):

$$\begin{aligned}\Delta T_{corr,sp}(x,y)&=\Delta T(x,y)-\delta \mathrm{T}_{drift}(x,y)\ \text{with}\ \delta \mathrm{T}_{drift}(x,y)\\&=\frac{\delta\omega_{drift}(x,y)}{2\pi\propto\bar{\gamma}B_0}\end{aligned} \tag{6}$$

2.3 | Phantom heating experiment

Experiments were performed on 1.5T and 3T clinical MR scanners (both Achieva; Philips Healthcare, Best, The Netherlands) equipped with a clinical MR-HIFU platform (Sonalleve MR-HIFU V2; Profound, Mississauga, Ontario, Canada). Images were acquired with a dual coil setup, using the integrated 2-element coil in the tabletop of the HIFU system and a 16-element flat array coil at 1.5T, or a 3-element pelvic coil at 3T, respectively. As illustrated in Figure 3A, the fast alternating acquisition of PRFS-MRT images

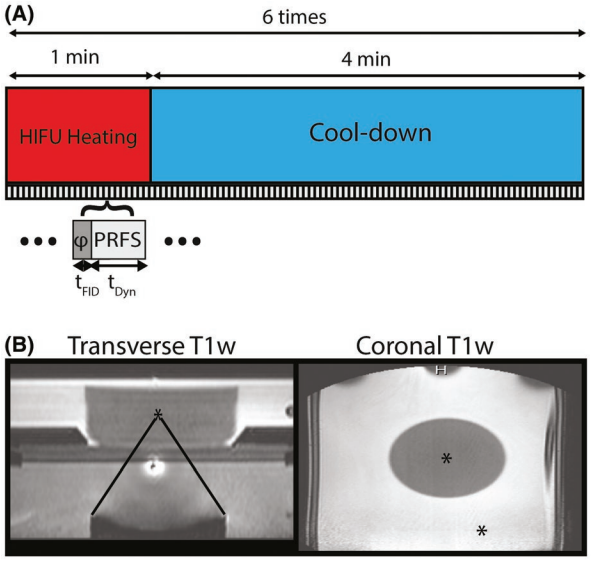

FIGURE 3 A, Illustration of the different timings of heating, cool-down, and the alternating acquisitions during the experiment. B, Transverse and coronal T1w image showing the experimental setup. The HIFU transducer, agar gel, and surrounding doped water can be seen. The black asterisks indicate where the 2 optical probes were positioned: 1 in the center of the HIFU cell and 1 in a nonheated area 15 cm from the center of the phantom

and FIDs were performed by using a sequence interleaving framework.[34] For PRFS-MRT, a multislice, multishot spoiled gradient recalled echo planar imaging (EPI) was used to acquire 3 coronal slices and 1 sagittal slice. The 3 coronal slices were as follows: 1 through the focus, 1 in the near, and 1 in the far field. For both 1.5T and 3T, common sequence parameter settings included binomial (1-2-1) water selective excitation, flip angle (FA) = 20°, EPI factor = 21, field of view (FOV) = 400 × 400 mm^2, acquired voxel size = 3.0 × 3.1 × 8 mm^3, and reconstructed voxel size = 2.5 × 2.5 × 8 mm^3. Some parameter settings were different: at 1.5T, TR = 100 ms, TE = 19 ms, and 1000 dynamics were acquired with all 4 slices acquired sequentially with t_{Dyn} = 1.6 seconds (4 slices × 0.4 seconds). Bandwidth was 1572.3 Hz/px in the readout direction and 64.5 Hz/px in the EPI phase-encoding direction.

At 3T, TE was shortened to TE = 16 ms to accommodate for the effects of main field inhomogeneity. Because of scanner limitations, TR = 200 ms, leading to t_{Dyn} = 3.2 seconds (4 slices × 0.8 seconds) and 500 dynamics to cover the same total duration. The bandwidth was 2807.4 Hz/px in the readout direction and 78.3 Hz/px in the EPI phase-encoding direction.

PRFS-MRT and FIDs were alternating such that 1 FID per coil element was acquired for every set of PRFS-MRT images. A nonselective block pulse was used to excite the full volume and generate an FID (Figure 1). Other parameter settings included: FA = 20° and a sampling window of

8 ms between 1.4 and 9.4 ms after excitation, during which 256 samples were acquired, leading to a total bandwidth of 32 kHz. Finally, gradient spoiling was used to minimize persisting signals.

MRT scanning was performed during 35 minutes to allow temperature monitoring of the entire heating experiment. HIFU sonications with a duration of 1 minute were followed by 4 minutes of cooling. This scheme was repeated 6 times, giving a 30-minute sequence of heating and cool-down cycles (see Figure 3A). HIFU sonications covered a 16-mm HIFU cell using a constant acoustic power of 40 W.[35] The phantom setup consisted of a large basin of 40 × 30 cm^2 filled with 8L manganese (Merck KGaA, Darmstadt, Germany) doped water (15 mg/kg), with a cylindrical 15-cm diameter agar/silica phantom positioned in the center to perform heating experiments (see Figure 3B). Two fiber optic thermometer probes (Luxtron m3300; LumaSense, Santa Clara, CA) were placed in the phantom, 1 probe was placed in the center of the HIFU sonication, and the other 15 cm off center in a nonheated region, as shown in Figure 3B. From a T1-weighted (T1w) scan, the position of the tip of the temperature probe was identified. The temperature map was planned through the identified position to ensure that the readout from the temperature map and optical probe coincided. Temperature readouts from the temperature probes were compared with the B_0 drift-corrected temperature maps for accuracy evaluation.

2.4 | In-vivo experiment

To confirm that the proposed method can detect and correct in-vivo B_0 field variations, an experiment was performed in a healthy volunteer without heating. The volunteer study was performed with the approval of the institutional review board of the University Medical Center of Utrecht (NL53099.041.15), and written informed consent was obtained from the volunteer.

At 1.5T, 4 MRT slices (3 coronal and 1 sagittal) were acquired in the lower leg of a healthy volunteer during 20 minutes, using the same alternating sequence and parameter settings with the 16-element receive coil used in the phantom experiment.

For referenceless PRFS thermometry, we used the near harmonic 2D referenceless approach proposed by Salomir et al to estimate background phase. This method is based on the constraint that any static magnetic field will fulfill the magnetostatic Maxwell equations and can thus be calculated when the phase on a circular contour placed in a nonheated region is known.[26] A synthetic phase background is then reconstructed within this circular contour using the 2D near harmonic approach. To initialize the process, a 100-mm diameter circular contour was placed within the boundaries of the phantom, which allowed to respect the condition that the used contour was positioned in an unheated field area. A 50-mm diameter circular contour was used in the *volunteer* experiment, as large as permitted by the size of the anatomy.

2.5 | Statistical analysis

For the phantom heating experiment to assess the accuracy of the 2 B_0 field drift correction methods, we calculated the temperature error ε_T (Equation 7):

$$\varepsilon_T = T_{measured} - T_{probe}. \quad (7)$$

Here, $T_{measured}$ is the temperature measured in a single voxel in the drift-corrected temperature map $\Delta T_{corr,0}$ or $\Delta T_{corr,sp}$ at the locations x and y where the temperature probes were located. T_{probe} is the temperature measured by the optical probes.

To evaluate the accuracy of the B_0 drift correction methods, the distribution of ε_T for all observed time points is presented in box plots. For the 2 correction methods, median and interquartile range (IQR) of the ε_T distribution are reported.

For the in-vivo results, to evaluate the error distribution of the B_0 drift correction methods, errors from all acquired voxels within a large ROI, from all time points, are presented in box plots; median and IQR of the distributions are reported.

For the phantom studies at 1.5T and 3T, resulting ε_T distributions were compared using Brown–Forsythe (variability) and Wilcoxon rank-sum (median) tests. The tested distributions were considered to be significantly different when $P < 0.05$. Similarly, the spatiotemporal temperature changes in vivo were compared using Brown–Forsythe and Wilcoxon rank-sum tests for data points from the ROI in which referenceless measurements of temperature change were available.

3 | RESULTS

3.1 | Phantom heating experiment

Figure 4A shows the field drift for each coil element, interpreted as temperature over the course of the phantom heating experiment for both field strengths. At 1.5T, during the experiment, all $\delta T_{drift,n}$ increased approximately linearly from 0°C to a range of 14.2°C to 16.9°C at 31 minutes. While at 3T, the impact of the B_0 field drift on the temperature measurement by the end of the experiment was in the range of 94°C to 99°C, depending on the coil element.

Figure 4B illustrates a typical example of reconstructed $\overline{\delta T_{drift,n}}$ and δT_{drift} (x, y) at the end of the heating experiment at both 1.5T and 3T. The average $\overline{\delta T_{drift,n}}$ correction map had a value of 15.7°C at 1.5T and 97.8°C at 3T. The spatial correction δT_{drift} (x, y) showcased values ranging between 14°C and 17°C at 1.5T, similar to the range of $\delta T_{drift,n}$ described in

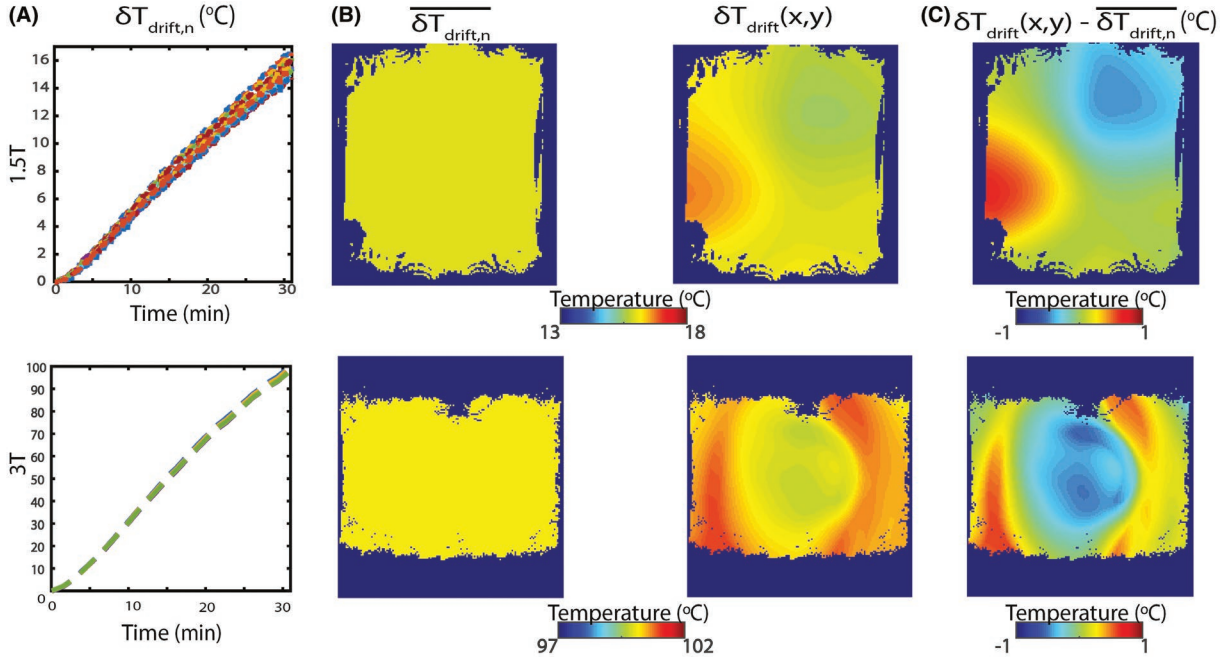

FIGURE 4 Typical examples of the temperature-interpreted B_0 drift $\delta T_{drift,n}$ as a function of time per coil element and field strength at both 1.5T (top) and 3T (bottom; A). Typical examples $\overline{\delta T_{drift,n}}$ and δT_{drift} (x, y) temperature map shown at 30 minutes time after the beginning of scanning at both 1.5T (top) and 3T (bottom; B); the color scale for both field strength have been windowed to the corresponding drift range (e.g., up to 18°C and 102°C) at 1.5T and 3T, respectively. Finally, subtraction of the spatially resolved correction and the applied 0th-order correction is shown to highlight the spatial dependence of the correction (C)

Figure 4A. While at 3T, the spatial variation of δT_{drift} (x, y) showcased values ranging between 93.5°C and 95.5°C. To further illustrate the spatial pattern detected by the method, a subtraction image of $\overline{\delta T_{drift,n}}$ and δT_{drift} (x, y) is shown in Figure 4C. A smooth apparent temperature gradient can be noticed at 1.5T whereas a concentric pattern was detected at 3T.

In Figure 5, typical examples of $\Delta T_{corr,0}$ and $\Delta T_{corr,sp}$ are shown at the 25-minute time point for 1.5T and 3T. At 1.5T, with both correction methods, the 16-mm HIFU cell was well visible. Once the spatially resolved correction was applied, the edges of the phantom appeared to be at a 0°C.

At 3T, with both correction methods, MRT was accurate in the center of the phantom within a 4-cm-diameter area and allowed clear identification of the HIFU sonication cell. However, strong artifacts were present at the edge of the phantom that neither of the methods were able to correct for, and errors ranging between –5°C and 5°C at the edge of the phantom typically remained.

At 1.5T, referenceless MRT, 0th-order correction, and spatially resolved correction all performed similarly, with a sonication location that was clearly identifiable on the temperature maps. At 3T, while the global aspect of the sonication seemed to be similar on all drift compensation techniques, the center of the sonications appeared to reach a lower temperature at the 25-minute time point for referenceless MRT, in the order of magnitude of 2°C, as compared to the 0th-order and spatially resolved corrections obtained from the FIDs.

In Figure 6A, the temperature readout from the optical probes at the matching locations of ΔT show with an improvement with both the $\Delta T_{corr,0}$ and $\Delta T_{corr,sp}$ correction. At both 1.5T and 3T, in the center of the HIFU cell with both 0th-order and spatially resolved correction, the optical probe readings compared to the measured PRFS temperature were in a close agreement with <2°C difference in all cases. This was further confirmed by the ε_T distribution. The distribution of ε_T for the entire experiment duration in the HIFU-heated area laid between –1°C to 1°C and –2°C to 1°C at 1.5T and 3T, respectively (see Figure 6E,F).

In the control area at 1.5T, Figure 6C shows an improvement of the spatial correction readout compared to the 0th-order correction. As shown in Figure 6E, the ε_T median and IQR from 0th-order were –1.28°C and 2.6°C, respectively, and were improved to a median of 0.4°C (Wilcoxon rank-sum, $P < 0.001$) with a 0.90°C IQR (Brown–Forsythe, $P < 0.001$). At 3T in the control area, no noticeable difference could be observed between the 0th-order and spatially resolved correction with a measured median of 2.1°C and IQR of 3.53°C in both cases (Figure 6F).

At 1.5T, the measured temperature changes with the referenceless method are in close agreement with $\Delta T_{corr,0}$ and $\Delta T_{corr,sp}$ and the optical probe readings (Figure 6C). However, after the 20-minute time point, the temperature

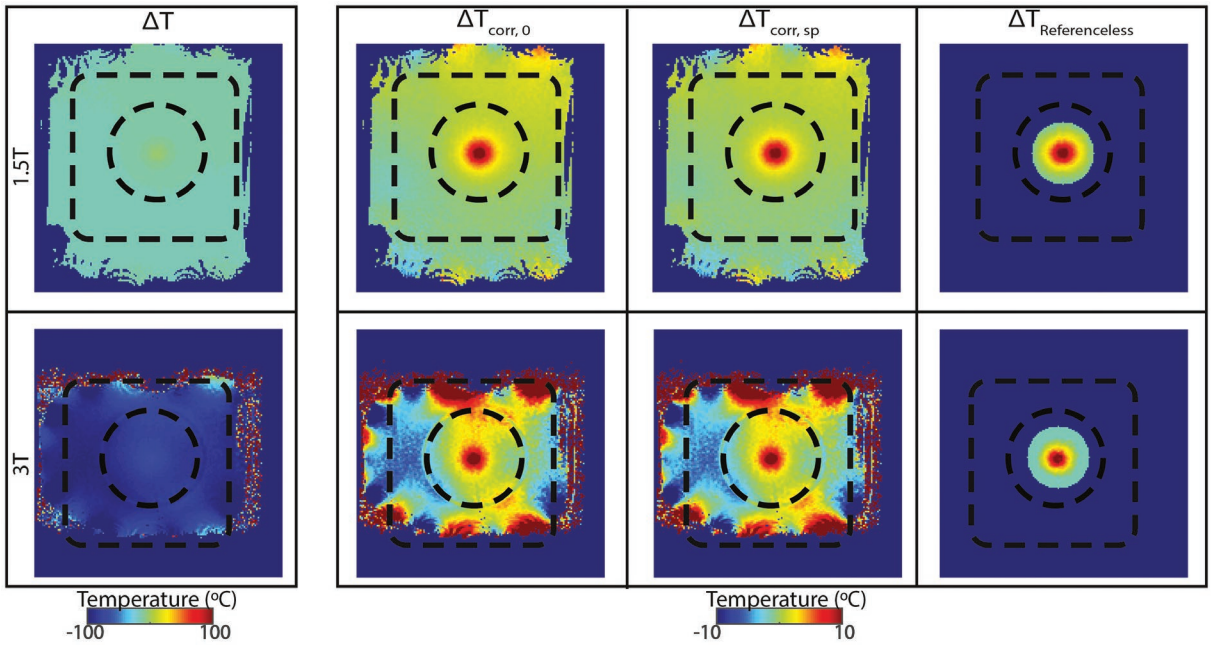

FIGURE 5 Coronal temperature maps through the focus obtained in the phantom experiments after 25 minutes of heating. From left to right, the noncorrected ΔT maps, and ΔT maps for 0th-order drift correction, spatially resolved correction and referenceless thermometry at both 1.5T (top) and 3T (bottom) are shown. The dashed black square dimensions are 250 × 250 mm. It represents, approximately, the reachable area with our HIFU system. The black dashed circles represent the boundaries of the agar phantom, which had a 150 mm diameter

change is underestimated progressively by up to 2°C. At 3T, the temperature change measured with the referenceless method was first overestimated within a range of 1°C to 2°C until the 17-minute time point. From this time point to the end, the temperature changes were underestimated between 1°C and 3°C (Figure 6D). At 1.5T, the ε_T distribution had a median of 0.03°C and an IQR of 0.4°C, which indicated larger variability than the 0th-order and spatially resolved corrections (Brown–Forsythe, $P < 0.001$). At 3T, the ε_T distribution had a median of –0.68°C with an IQR of 1.5°C, again indicating larger variability than the 0th-order and spatially resolved corrections (Brown–Forsythe, $P < 0.001$).

3.2 | In-vivo experiment

To illustrate the need for drift correction, and the effectiveness of applied corrections, maps of the maximum absolute temperature error observed during the experiment are shown in Figure 7. Without correction, values up to 14°C were observed with a craniocaudal gradient ranging between 13°C and 14°C. With the 0th-order correction, an overall maximum error of 1.5°C with values up to 2°C at the edges of the leg can be noticed. The spatially resolved method allowed the lowest error values under 1.5°C. The temperature error over time for both methods (Figure 8A) shows that a temperature error within –1°C to 1°C could be maintained. However a clear 1°C offset is present between the 2 methods, with the spatially resolved correction method close to the 0°C line. Summarizing the temperature estimates from all locations in the ROI for all time points in box plots, Figure 8B shows that the median temperature estimate was –4.3°C with an IQR of 9.31°C without correction, with a substantial improvement by the 0th-order correction method to a median of 0.75°C with an IQR of 0.96°C. Finally, the spatially resolved correction allowed the lowest errors with a median at 0.33°C and an IQR of 0.80°C.

In the volunteer experiment, the maximum errors for the referenceless method were larger than those observed for the FID-based corrections (Figure 7). A strong artifact originating from the bony structure close to the reference contour has led to these above 3°C artifact present in the overall ROI. Figure 8A shows a clear offset increasing from 1°C to 2°C during the larger part of the experiment. It was also observed that precision was lower for referenceless thermometry than for the FID-based corrections, with a median of 1.89 (Wilcoxon rank-sum, $P < 0.001$) and IQR of 2.36°C (Brown–Forsythe, $P < 0.001$; Figure 8B).

4 | DISCUSSION

Thermal therapy monitoring using PRFS temperature mapping requires an efficient spatial B_0 drift correction to maintain an adequate accuracy (range of ±1°C). As demonstrated in this study, this can be achieved by correcting for drift using alternating PRFS thermometry and multichannel FID acquisitions. The method allowed to

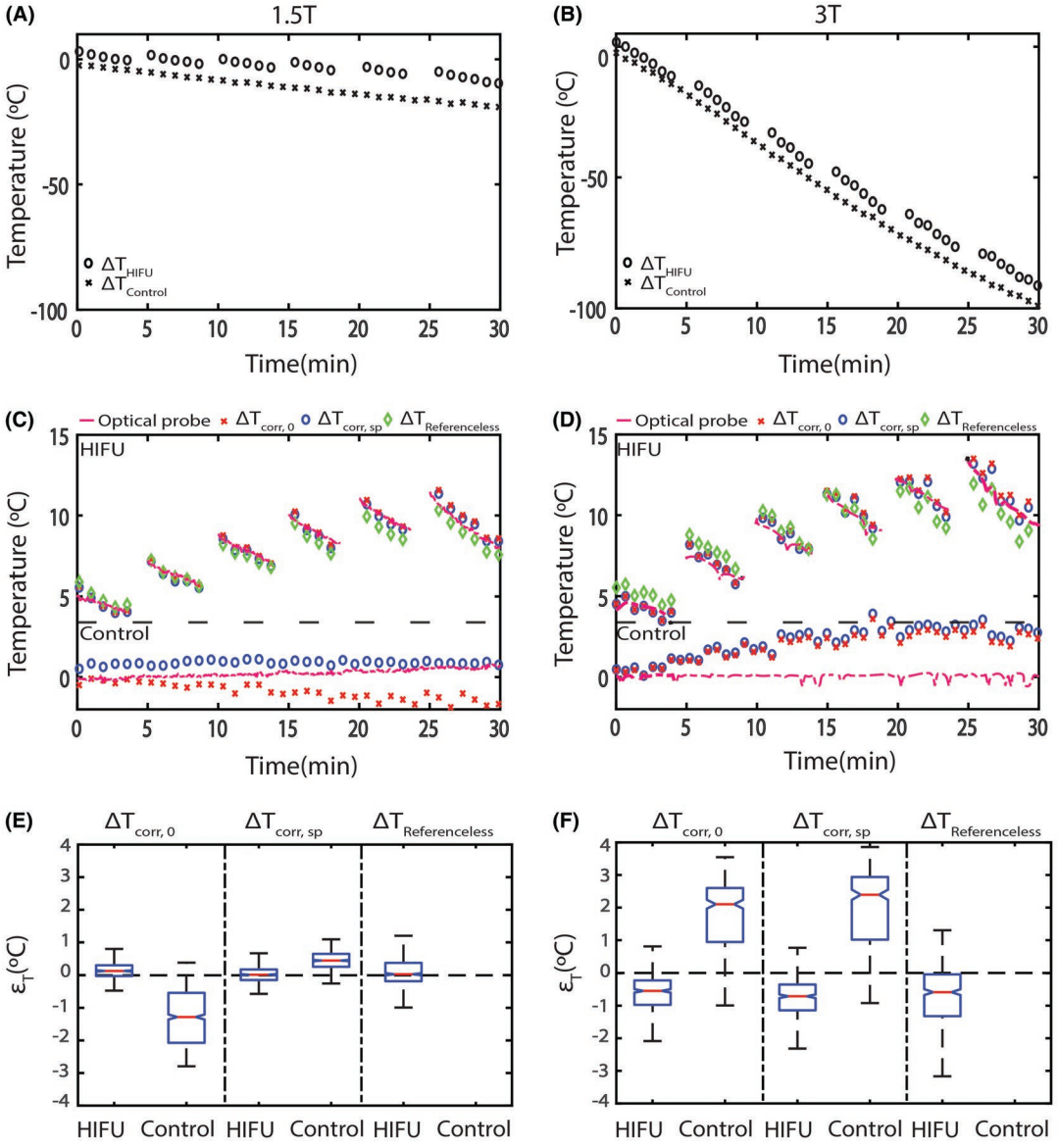

FIGURE 6 Comparison of uncorrected ΔT measurements in the center of the HIFU cell and in the control area at 1.5T (A) and 3T (B). Optical probe temperature readings are compared with $\Delta T_{corr,0}$, $\Delta T_{corr,sp}$, and $\Delta T_{referenceless}$ for both locations (HIFU and control) at 1.5T (C) and 3T (D). The accuracy of 0th-order correction, spatially resolved correction, and referenceless thermometry are shown in terms of the temperature error ε_T for (E) 1.5T and (F) 3T. With the referenceless method, measurements were not possible in the control area. Because of interference with the US waves, the optical probe data for the heated area is only shown for the cooling periods in (A), (B), (C), and (D)

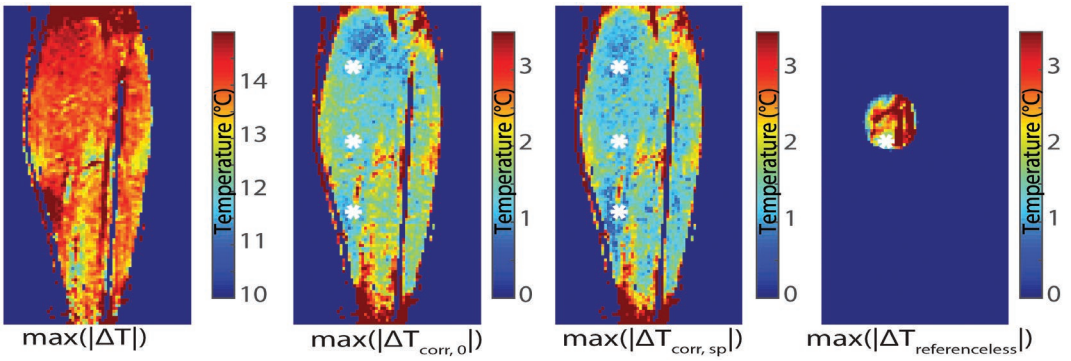

FIGURE 7 Coronal images through the lower leg of a volunteer, showing maps of the maximum temperature error incurred during the entire experiment at 1.5T. From left to right: without correction, 0th-order correction, spatially resolved correction, and with referenceless thermometry

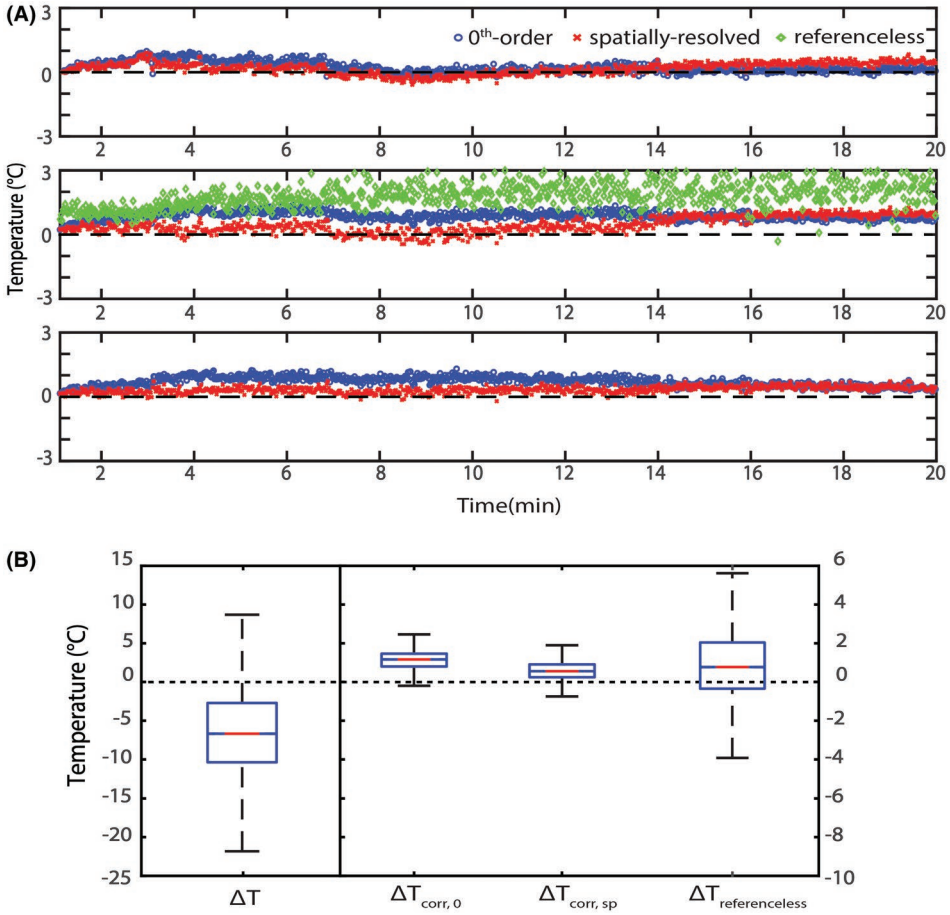

FIGURE 8 A, Typical examples of temperature change as a function of time in 3 locations (indicated by the white asterisk in panel a), with the 0th-order correction (red), spatially resolved (blue), and referenceless (green) methods. For reference, a dotted line at 0°C is shown. B, The observed spatiotemporal temperature distribution for all acquired slices, from left to right, without correction, 0th-order correction, spatially resolved correction, and with the referenceless method. Distribution of all points encompassed within the same ROI as the one used for referenceless MRT were used in the analysis

account for spatial variation in the B_0 drift correction and maintain this accuracy level over the 30-minute duration of the experiment. The proposed method neither required user interaction nor were adaptations to the hardware of the MR-HIFU setup needed.

The approach bears similarities to using field probes for monitoring the spatiotemporal variation of the B_0 field of the system.[29,31] However, individual field probes require a spatial interpolation because they measure field variation in locations outside the body, whereas the use of the imaging array and its individual sensitivity profile allows to directly measure B_0 variation from the body itself. Inherently, by comparing the results between the 16-element setup at 1.5T and 3-element setup at 3T (Figure 6E,F), it can be established that the efficiency of the correction methods depends on the number of coil elements and the associated receive field of the individual and overlapping coil profiles.[36] Although superior spatial B_0 drift correction can be achieved using a high number of coil elements, in practice, these arrays are not generally available on MR-HIFU systems because these systems have additional design constraints. Therefore, a combination of existing techniques using the phase images (e.g., referenceless) with the proposed method or with external field probes could be of interest.

The comparison between the FID-based methods and referenceless MRT showed that in the phantom study, the FID-based method performed as well as the referenceless at 1.5T. The accuracy of referenceless thermometry was poorer at 3T, and it did not allow temperature monitoring in the control area. In the in-vivo experiment, referenceless MRT precision was poorer than with the FID-based methods. It can be argued that referenceless is better suited for large organs with a relatively smooth background phase (e.g., brain and liver[24,37-39]) than for challenging anatomy (e.g., bowel, bone).

With the referenceless approach, positioning of the ROI within the organ boundaries and an area that is not affected by any phase changes attributable to heating is key to avoid

corruption of the reconstructed phase background.[24] However, in the context of mild hyperthermia, the measured phase within the surrounding ROI might get corrupted because of heat diffusion from the large, targeted heated volume.

The FID-based method relies on the presence of nonheated tissue, where the only source of phase change is the field drift.[40] In our study, the use of a nonselective full-volume excitation reduces the influence of the heated volume: first, by making use of a large pool of nonheated water protons and, in vivo, by adding a large pool of lipid protons. The frequency shift of the fat signal is independent of temperature, because hydrogen bonds are absent in the fat aliphatic chains. Hence, only susceptibility and B_0 drift affect the frequency of the fat signal.[19] In the proposed implementation, the excitation pulse used for the acquisition of the FIDs is chemically broadband and spatially nonselective. Thus, including the fat signal enlarges the pool of spins experiencing only the B_0 drift contributing to the FID signals.

Still, this method would be limited if the heated volume becomes too large and starts to significantly affect the FID signal, as was shown for correction based on slice-selective FID phase navigators.[32] For the experiments presented here, the heated volume was relatively small and the performance of B_0 drift correction did not seem to be affected. However, this limitation, especially in the context of radiofrequency (RF) mild hyperthermia, where the volume of heated tissue is larger, should be investigated. Similar experiments with regional heating should be carried out to evaluate whether the use of nonselective FIDs still allows accurate drift correction in this context (e.g., by RF heating or HIFU).[41]

In principle, B_0 drift can also lead to slice position shifts and in plane distortions.[42] In this study, with the sequence used, no slice or voxel shift was noticed. In principle, however, using this method could also offer the possibility to correct for in-plane distortions and shifts as previously demonstrated with a similar approach by Versluis et al.[43]

For use in therapy guidance and especially for mild hyperthermia, where temperatures are intended to be kept within tight boundaries,[44] it is crucial that drift correction can be applied in real time to correct MR temperature mapping. When feedback-controlled heating methods are used, MRT is used to control the energy delivery and therefore requires a short latency.[45] The suggested acquisition and processing scheme has the potential to fulfill these real-time requirements. As implemented, the acquisition of the FID required only 1 extra TR per dynamic, and the spatial unfolding of the signal relies on a previously acquired sensitivity scan. The only processing steps that would need to take place in real time are the linear fit and the calculation of the weighted sum. In the Matlab (The MathWorks, Inc., Natick, MA) implementation, these 2 steps were achieved in less than 0.1 second. In addition, the full-volume nonselective excitation yielded FIDs with high signal-to-noise ratio both at 1.5T and 3T.

Some limitations of this study are worth mentioning. At the edge of the FOV, larger residual drift terms were present, which were not corrected by the proposed correction method. These variations were present in the uncorrected drift maps and were not sufficiently resolved by the coil sensitivity map to be corrected. Further work should be carried out to investigate whether this effect is still present in vivo and whether it can be corrected with a higher number of coil elements. In this study, the created temperature rise was slightly higher than the typical temperature rise with mild hyperthermia; however, the performance of the method did not seem to be affected. All experiments carried were performed in a phantom or in stationary anatomy. Respiratory, cardiac, and incidental patient motion are known to affect MRT[34] and are likely to affect the acquired FID signal. Similar FID phase navigators or navigators based on the central k-space point or profile have been proposed for motion correction.[35] The suggested implementation allows a high degree of freedom for acquisition of the FID with a superior frame rate to enable capturing changes in motion state. Further work should be carried out to develop strategies to extract drift information in case of motion, or even extract drift and motion estimates simultaneously. In this study, the suggested approach was evaluated in the lower leg of 1 healthy volunteer without HIFU heating. Further work should be carried out to investigate whether the proposed method still performs robustly in body areas such as the abdomen, where multiple air-to-tissue boundaries are encountered. In addition, the accuracy and precision of the method during in-vivo MR-HIFU heating should be investigated.

In conclusion, using individual receive coil sensitivity profiles combined with fast alternating FID acquisitions allows to spatially compensate B_0 drift in PRFS-based MRT. Acquisition of the FIDs were sufficiently fast to not compromise the temporal resolution of the PRFS-MRT and allowed to achieve sufficient temperature precision for mild hyperthermia guidance (range, ± 1°C).

ACKNOWLEDGMENTS

Part of this work was funded by the European Union Seventh Framework Programme (FP7/2007–2013) under grant agreement 603028 (iPaCT project). The authors thank Jochen Keupp and Peter Koken for providing the tools to implement the interleaved framework acquisition on our system.

CONFLICT OF INTEREST

Edwin Heijman is an employee of Philips Research.

ORCID

Cyril J. Ferrer http://orcid.org/0000-0001-9804-5626

REFERENCES

1. Napoli A, Anzidei M, Ciolina F, et al. MR-guided high-intensity focused ultrasound: current status of an emerging technology. *Cardiovasc Intervent Radiol*. 2013;36:1190–1203.
2. Elias WJ, Huss D, Voss T, et al. A pilot study of focused ultrasound thalamotomy for essential tremor. *N Engl J Med*. 2013;369:640–648.
3. Hurwitz MD, Ghanouni P, Kanaev SV, et al. Magnetic resonance-guided focused ultrasound for patients with painful bone metastases: phase III trial results. *J Natl Cancer Inst*. 2014;106:dju082.
4. Kim YS. Advances in MR image-guided high-intensity focused ultrasound therapy. *Int J Hyperthermia*. 2015;31:225–232.
5. Rodrigues DB, Stauffer PR, Eisenbrey J, Beckhoff V, Hurwitz MD. Oncologic applications of magnetic resonance guided focused ultrasound. In: Wong JYC, Schultheiss TE, Radany EH, eds. *Advances in Radiation Oncology*. Cham, Switzerland: Springer International; 2017:69–108.
6. Toccaceli G, Delfini R, Colonnese C, Raco A, Peschillo S. Emerging strategies and future perspective in neuro-oncology using transcranial focused ultrasonography technology. *World Neurosurg*. 2018;117:84–91.
7. Staruch RM, Hynynen K, Chopra R. Hyperthermia-mediated doxorubicin release from thermosensitive liposomes using MR-HIFU: therapeutic effect in rabbit Vx2 tumours. *Int J Hyperthermia*. 2015;31:118–133.
8. De SM, Heijman E, Langereis S, Hijnen NM, Grüll H. Magnetic resonance imaging of high intensity focused ultrasound mediated drug delivery from temperature-sensitive liposomes: an in vivo proof-of-concept study. *J Control Release*. 2011;150:102–110.
9. Chu W, Staruch RM, Pichardo S, et al. Magnetic resonance e guided high-intensity focused ultrasound hyperthermia for recurrent rectal cancer: MR thermometry evaluation and preclinical validation. *Int J Radiat Oncol Biol Phys*. 2016;95:1259–1267.
10. Edwin Heijman E, Sin Yuin Yeo SY, Lukas Sebeke L, et al. Volumetric hyperthermia of soft tissue sarcoma using MR guided high intensity focused ultrasound: case report. In *Proceedings of the 6th International Symposium on Focused Ultrasound*, McLean, VA, 2018. p. CA35.
11. Maloney E, Hwang JH. Emerging HIFU applications in cancer therapy. *Int J Hyperthermia*. 2014;6736:1–8.
12. Rieke V, Pauly KB. MR thermometry. *J Magn Reson Imaging*. 2008;27:376–390.
13. Kuroda K. Non-invasive MR thermography using the water proton chemical shift. *Int J Hyperthermia*. 2005;21:547–560.
14. Salomir R, Vimeux FC, De Zwart JA, Grenier N, Moonen C. Hyperthermia by MR-guided focused ultrasound: accurate temperature control based on fast MRI and a physical model of local energy deposition and heat conduction. *Magn Reson Med*. 2000;43:342–347.
15. Partanen A, Yarmolenko PS, Viitala A, et al. Mild hyperthermia with magnetic resonance-guided high-intensity focused ultrasound for applications in drug delivery. *Int J Hyperthermia*. 2012;28:320–336.
16. Datta NR, Ordóñez SG, Gaipl US, et al. Local hyperthermia combined with radiotherapy and-/or chemotherapy: recent advances and promises for the future. *Cancer Treat Rev*. 2015;41:742–753.
17. De Poorter J, De Wagter C, De Deene Y, Thomsen C, Ståhlberg F, Achten E. Noninvasive MRI thermometry with the proton resonance frequency (PRF) method: in vivo results in human muscle. *Magn Reson Med*. 1995;33:74–81.
18. El-sharkawy AM, Morgan RH, Science R, Hopkins J. Monitoring and correcting spatio-temporal variations of the MR scanner's static magnetic field. *MAGMA*. 2007;19:223–236.
19. Shmatukha AV, Harvey PR, Bakker C. Correction of proton resonance frequency shift temperature maps for magnetic field disturbances using fat signal. *J Magn Reson Imaging*. 2007;25:579–587.
20. Kuroda K, Oshio K, Chung AH, Hynynen K, Jolesz FA. Temperature mapping using the water proton chemical shift: a chemical shift selective phase mapping method. *Magn Reson Med*. 1997;38:845–851.
21. Soher BJ, Wyatt C, Reeder SB, MacFall JR. Noninvasive temperature mapping with MRI using chemical shift water-fat separation. *Magn Reson Med*. 2010;63:1238–1246.
22. Svedin BT, Payne A, Parker DL. Respiration artifact correction in 3D PRF MR thermometry using phase navigators. *Magn Reson Med*. 2016;76:206–213.
23. Hey S, Maclair G, De Senneville BD, et al. Online correction of respiratory-induced field disturbances for continuous MR-thermometry in the breast. *Magn Reson Med*. 2009;61:1494–1499.
24. De Senneville BD, Roujol S, Moonen C, Ries M. Motion correction in MR thermometry of abdominal organs: a comparison of the referenceless vs. the multibaseline approach. *Magn Reson Med*. 2010;64:1373–1381.
25. Grissom WA, Lustig M, Holbrook AB, Rieke V, Pauly JM, Butts-Pauly K. Reweighted $\ell 1$ referenceless PRF shift thermometry. *Magn Reson Med*. 2010;64:1068–1077.
26. Salomir R, Viallon M, Kickhefel A, et al. Reference-free PRFS MR-thermometry using near-harmonic 2-D reconstruction of the background phase. *IEEE Trans Med Imaging*. 2012;31:287–301.
27. Zou C, Shen H, He M, Tie C, Chung YC, Liu X. A fast referenceless PRFS-based MR thermometry by phase finite difference. *Phys Med Biol*. 2013;58:5735–5751.
28. Zou C, Tie C, Pan M, et al. Referenceless MR thermometry—a comparison of five methods. *Phys Med Biol*. 2017;62:1–16.
29. Duerst Y, Wilm BJ, Dietrich BE, et al. Real-time feedback for spatiotemporal field stabilization in MR systems. *Magn Reson Med*. 2015;73:884–893.
30. Andersen M, Hanson LG, Madsen KH, et al. Measuring motion-induced B0-fluctuations in the brain using field probes. *Magn Reson Med*. 2016;75:2020–2030.
31. Hernandez D, Kim KS, Michel E, Lee SY. Correction of B0 drift effects in magnetic resonance thermometry using magnetic field monitoring technique. *Concepts Magn Reson Part B Magn Reson Eng*. 2016;46B:81–89.
32. Dadakova T, Krafft AJ, Korvink JG, Meckel S, Bock M. PRF Thermometry for monitoring small temperature changes during very long thermal therapies: field drift compensation using FID navigators. In Proceedings of the 24th Annual Meeting of the ISMRM, Singapore, 2016.
33. Pruessmann KP, Weiger M, Scheidegger MB, Boesiger P. SENSE: sensitivity encoding for fast MRI. *Magn Reson Med*. 1999;3:952–962.

34. Henningsson M, Mens G, Koken P, Smink J, Botnar RM. A new framework for interleaved scanning in cardiovascular MR: application to image-based respiratory motion correction in coronary MR angiography. *Magn Reson Med*. 2015;696:692–696.
35. Köhler MO, Mougenot C, Quesson B, et al. Volumetric HIFU ablation under 3D guidance of rapid MRI thermometry. *Med Phys*. 2009;36:3521–3535.
36. Glockner JF, Hu HH, Stanley DW, Angelos L, King K. Parallel MR imaging: a user's guide. *Radiographics*. 2005;25:1279–1297.
37. Rieke V, Instrella R, Rosenberg J, et al. Comparison of temperature processing methods for monitoring focused ultrasound ablation in the brain. *J Magn Reson Imaging*. 2013;38:1462–1471.
38. Grissom WA, Rieke V, Holbrook AB, et al. Hybrid referenceless and multibaseline subtraction MR thermometry for monitoring thermal therapies in moving organs. *Med Phys*. 2010;37:5014–5026.
39. McDannold N, Tempany C, Jolesz F, Hynynen K. Evaluation of referenceless thermometry in MRI-guided focused ultrasound surgery of uterine fibroids. *J Magn Reson Imaging*. 2008;28:1026–1032.
40. Rieke V, Vigen KK, Sommer G, Daniel BL, Pauly JM, Butts K. Referenceless PRF shift thermometry. *Magn Reson Med*. 2004;51:1223–1231.
41. Paulides MM, Stauffer PR, Neufeld E, et al. Simulation techniques in hyperthermia treatment planning. *Int J Hyperthermia*. 2013;29:346–357.
42. Reichenbach JR, Venkatesan R, Yablonskiy DA, Thompson MR, Lai S, Haacke EM. Theory and application of static field inhomogeneity effects in gradient-echo imaging. *J Magn Reson Imaging*. 1997;7:266–279.
43. Versluis MJ, Sutton BP, De Bruin PW, Börnert P, Webb AG, Van Osch MJ. Retrospective image correction in the presence of nonlinear temporal magnetic field changes using multichannel navigator echoes. *Magn Reson Med*. 2012;68:1836–1845.
44. Craciunescu OI, Stauffer PR, Soher BJ, et al. Accuracy of real time noninvasive temperature measurements using magnetic resonance thermal imaging in patients treated for high grade extremity soft tissue sarcomas. *Med Phys*. 2009;36:4848–4858.
45. Partanen A, Yarmolenko PS, Viitala A, et al. Mild hyperthermia with magnetic resonance-guided high-intensity focused ultrasound for applications in drug delivery. *Int J Hyperthermia*. 2012;28:320–336.

How to cite this article: Ferrer CJ, Bartels LW, van der Velden TA, et al. Field drift correction of proton resonance frequency shift temperature mapping with multichannel fast alternating nonselective free induction decay readouts. *Magn Reson Med*. 2020;83:962–973. https://doi.org/10.1002/mrm.27985